Analysis of the Locking Range of Rationally Synchronized Oscillators With High Reference Signal Power

Miguel Fernández García, *Member, IEEE*, Samuel Ver Hoeye, *Member, IEEE*, Carlos Vázquez, George Roberto Hotopan, René Camblor, and Fernando Las Heras, *Senior Member, IEEE*

***Abstract*—In this paper an in-depth study of the behavior of rationally synchronized oscillators (RSO) is presented. The circuit is optimized in order to achieve a broad synchronization bandwidth with low reference signal power through the selection of the adequate harmonic content. The nonlinear dynamics of the RSO is analyzed, focusing on the different bifurcation points which delimit the locking range when high reference signal power is considered. An RSO prototype with rational synchronization ratio $r = 3/5$, autonomous frequency $f_o = 3$ GHz and reference signal frequency $f_r = 5$ GHz has been manufactured and experimentally characterized, demonstrating a good agreement with simulation results.**

***Index Terms*—Bifurcation detection, microwave oscillators, nonlinear optimization, rational synchronization.**

I. Introduction

In modern microwave communication systems, carrier signals with good frequency stability and phase noise properties are required. These signals are commonly generated by systems based on the use of synthesized oscillators. However, when several carrier signals with different frequencies are needed, the complexity and the cost of the system rapidly increase with the number of required synthesized oscillators.

A different approach in which each carrier signal is generated by a rationally synchronized oscillator (RSO) [1] can be applied, in order to simplify the system and reduce its cost. The RSO circuit described in this work is based on a single transistor and a reduced number of components and can be easily implemented in microstrip technology. Therefore, it is a compact and low-cost circuit with a reduced power consumption, which can be integrated together with radiating elements in order to design low-cost active antennas.

With this alternative, one synthesized oscillator provides the reference signal to all of the RSO circuits in the system. Since all of the RSO circuits share the synchronization signal, the rational relation r between the free-running frequency f_o and the reference signal frequency f_r, expressed as $r = f_o/f_r = M/N$, is different for each RSO, leading to rationally related carriers. With this configuration, all of the RSO output signals have a known fixed phase relation with the reference signal, reached through the synchronization between the Nth harmonic component of the self-oscillation signal and the Mth harmonic component of the reference signal, generated by the nonlinear characteristic of the active device.

Rational synchronization has been described in technical literature as a method for the improvement of the oscillator phase noise and for the implementation of low-cost rational frequency dividers [2]–[5] and multicarrier Tx/Rx systems [6]. However, there are few works in which the complex dynamics of RSOs is analyzed. The main drawback of the RSO is the high reference signal power that is needed in order to achieve a practical value of the synchronization bandwidth. This problem increases for high synchronization orders, with N, $M > 2$, and must be taken into account when several RSO circuits share the same reference signal. In this case, unless high reference signal power is considered, the synchronization phenomenon is only observable through the detection of noisy precursors [7], and it has no practical interest.

To overcome this limitation, some techniques for the enlargement of the locking range of RSOs and analog frequency dividers have been developed. In [2] and [4], the locking range is enlarged through the addition of low-frequency feedback loops. Thus, the number of components and the complexity of the circuit are increased. In addition, the required reference signal power is still relatively high. On the other hand, the work in [1] describes the optimization of the RSO synchronization bandwidth by means of the control of the harmonic content of the circuit, i.e., the amplitudes of the synchronizing harmonics. In this case, a practically usable locking range has been achieved, with $N = 3$, $M = 4$, -10 dBm reference signal power, and without additional circuitry. Finally, in [8], it is shown that the required reference signal power can be considerably reduced through the adequate selection of the circuit working regime, which is forced to be close to a Hopf bifurcation point. A strong amplification effect is generated around the frequency of the input

This work was supported in part by the "Ministerio de Ciencia e Innovación" of Spain and "FEDER", under Project IPT-2011-0951-390000 (TECNIGRAF), Project TEC2011-24492 (ISCAT), Project TEC2008-01638 (INVEMTA), Project "CONSOLIDER-INGENIO CSD2008-00068" (TERASENSE), and Frant AP2009-0438, by the "Plan de Ciencia y Tecnología" (PCTI/FEDER-FSE) of the "Gobierno del Principado de Asturias", under Project EQUIP08-06, Project FC09-COF09-12, Project EQUIP10-31, Project PC10-06, and Grant BP10-031, and by the "Catedra Telefonica-Universidad de Oviedo."

The authors are with the Signal Theory and Communications Area, Department of Electrical Engineering, University of Oviedo, Gijon E-33204, Spain (e-mail: mfgarcia@tsc.uniovi.es).

reference signal to enlarge the amplitude of its harmonic components. Hence, the reference signal power required to achieve a particular synchronization bandwidth is considerably reduced.

In order to analyze the complex nonlinear dynamics of autonomous circuits and systems under synchronized operation regime, several techniques have been proposed, both in time [9], [10] and frequency domains. In this work, efficient harmonic balance-based techniques are applied to the analysis of RSO circuits. The circuit synchronization bandwidth is optimized through the control of the harmonic content of the circuit [1]. The locking range is analyzed versus the amplitude of the Nth harmonic component of the autonomous signal V_o^N and the Mth harmonic component of the reference signal V_r^M, calculating the synchronization loci by means of harmonic balance simulations based on the use of an auxiliary generator [11], [12]. The stability of the synchronized solutions is efficiently analyzed through the envelope transient technique combined with the use of an auxiliary generator, which is used to initialize the system state variables [13]–[18].

After optimizing the circuit, the nonlinear dynamics of the RSO is exhaustively analyzed. The influence of the reference signal power on the behavior of the synchronized solutions is carefully studied, paying special attention to the bifurcations that limit the stable operation ranges of the RSO. In addition, the different unsynchronized solutions of the circuit are characterized as a function of the reference signal parameters. The data provided by the performed analysis are used to obtain a detailed bifurcation map that describes the overall RSO behavior versus the frequency and the power of the reference signal. To our knowlege, this is the first time that such in-depth study of the nonlinear dynamics of an RSO is reported.

This paper is organized as follows. In Section II, the topology of the RSO is presented, and the design and optimization process is described. Section III is devoted to the optimization of the circuit locking range through the control of its harmonic content. The nonlinear dynamics exhibited by the RSO when high reference signal power values are considered is analyzed in detail in Section IV. Finally, in Section V, some key aspects regarding the manufacturing of the circuit are described and the experimental data, including phase noise measurements, are presented.

II. RSO Design and Optimization

A. Topology

The RSO topology is depicted in Fig. 1. It is based on a single ultralow-noise PHEMT Avago ATF-36073 transistor. The feedback network placed at the source port provides the oscillation conditions and includes a varactor diode to tune the frequency f_o of the self-oscillation signal. The reference signal, with frequency f_r, power P_r, and arbitrary phase ϕ_r is provided through a conventional $\lambda/4$ coupled-line bandpass filter connected to the transistor gate port. Another bandpass filter with central frequency f_o is placed at the drain port to select the output signal of the circuit. The frequency response of both filters, obtained through an electromagnetic simulation based on the Method of Moments (MoM), is represented in Fig. 2, together with the experimental data. Note that each filter provides a rejection value greater than 20 dB at the center frequency of the other one.

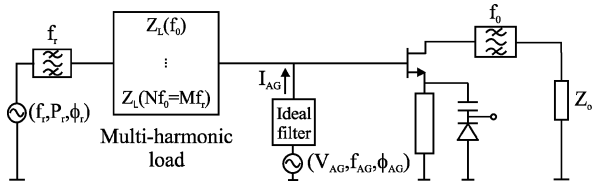

Fig. 1. Topology of the RSO with inclusion of an auxiliary generator for optimization purposes.

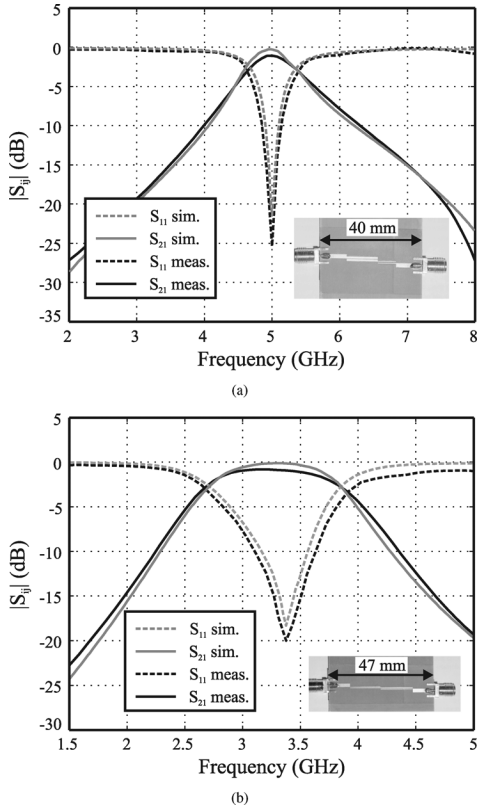

Fig. 2. Simulated and measured frequency response of the filters. (a) Input filter. (b) Output filter.

Moreover, due to the characteristics of the considered application, the bandwidth of the filters is not a limiting factor. A multiharmonic load [12], [19], based on an arbitrarily modulated width microstrip transmission line [8], [20], is also connected at the gate port of the transistor, for optimization purposes. The same type of structure is used for the implementation of the dc-bias networks [20], which must present high input impedance around the frequencies of all of the considered harmonic components of the self-oscillation and the reference signal, $f = k \times f_o$, $k = \{1, \ldots, N\}$ and $f = j \times f_r$, $j = \{1, \ldots, M\}$, respectively. The MoM simulation data and the measured frequency response of the dc-bias network are shown in Fig. 3. Since the input impedance of the dc-feed network is not matched to 50 Ω, the network has been connected to the center of a 30-mm-length microstrip transmission line, with characteristic impedance $Z_o = 50\,\Omega$ (see inset picture in Fig. 3). The frequency response of the dc-bias network is then measured by evaluating the transmission coefficient S_{21} between the two terminals of the 50-Ω transmission line [20].

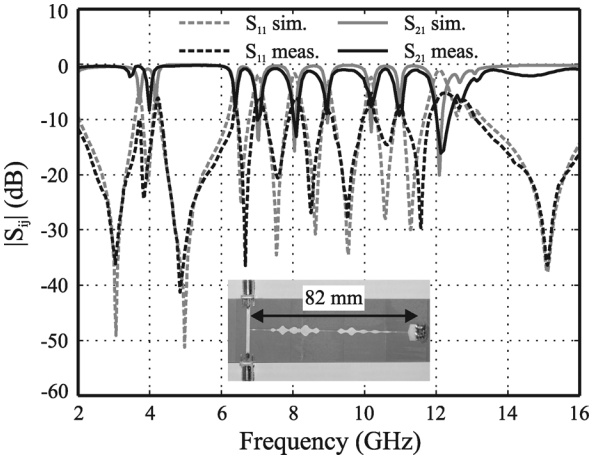

Fig. 3. Simulated and measured frequency response of the dc-bias network based on an arbitrarily width modulated microstrip transmission line.

B. Design and Optimization

The frequency f_o and the amplitude V_o of the first harmonic component of the autonomous signal are imposed through an optimization process in which several parameters of the circuit are modified in order to satisfy the nonperturbation condition of the auxiliary generator $Y_{\rm AG} = I_{\rm AG}/V_{\rm AG} = 0$ [11]–[13]. As shown in Fig. 1, the auxiliary generator is connected at the gate port of the transistor and operates at the frequency $f_{\rm AG} = f_o$, with amplitude $V_{\rm AG} = V_o$ and phase ϕ_{AG}.

The rational synchronization regime combines features of the harmonic [2], [4], [21]–[23] and subharmonic [3], [24], [25] synchronization regimes. Therefore, for a constant value of the reference signal power P_r, the locking range depends on the amplitudes of the first and Nth harmonic components of the autonomous signal, V_o and V_o^N respectively, the amplitude of the Mth harmonic component of the reference signal V_r^M and the oscillator quality factor Q_L.

In order to analyze the locking range versus the harmonic content of the circuit, the values of V_o and Q_L are fixed, with a reference signal power value $P_r = -10$ dBm. The quality factor can be expressed as [26]

$$Q_L = \frac{f_o}{2G_L}\frac{\partial Y^i_{\rm AG}}{\partial f}\bigg|_{f=f_o} \tag{1}$$

where G_L is the load conductance and $Y^i_{\rm AG}$ represents the imaginary part of the admittance evaluated at the gate port of the transistor, where the auxiliary generator is connected. In a first step, the value of Q_L is minimized in a multitone harmonic balance-based optimization process in which two copies of the circuit are involved. Each RSO copy has its own auxiliary generator, with identical amplitude and phase, but different frequency, $f_{\rm AG,1} = f_o$ and $f_{\rm AG,2} = f_o + \Delta f$. Because the value of G_L is constant, the oscillator quality factor can be easily optimized by minimizing the difference $Y^i_{\rm AG,2}(f_o + \Delta f) - Y^i_{\rm AG,1}(f_o)$. Note that the phase noise increases as the oscillator quality factor reduces. Therefore, the value of Q_L must be carefully selected. After the optimization, it is kept constant along the rest of the design process by adding a perturbation current source with frequency $f_p = f_o + \Delta f$ and amplitude $I_p = \epsilon$, sufficiently low to not disturb the steady-state autonomous solution of the circuit. This current source is connected at the gate port of the transistor, in parallel with the auxiliary generator, allowing the control of the admittance existing at this point, at frequency $f_o + \Delta f$. Since the nonperturbation condition of the auxiliary generator imposes that $Y_{\rm AG}(f_o) = 0$, the quality factor of the oscillator is kept constant by fixing the admittance seen by the perturbation generator. The computational cost of solving the harmonic balance equations system is higher in the case of using two circuits with two auxiliary generators because of the high value of their amplitudes. When using two copies of the circuit, two auxiliary generators with frequencies $f_{AG,\,1} = f_o$ and $f_{\rm AG,\,2} = f_o + \Delta f$ are considered. In this case, the harmonic balance frequency basis is composed by two tones, at frequencies f_o and $f_o + \Delta f$, and their first eight harmonic components. Therefore, the frequency basis contains 16 time-varying and two dc components. On the other hand, with the proposed approach based on only one copy of the circuit and a small amplitude current generator, working at frequency $f_p = f_o + \Delta f$, the harmonic balance frequency basis is also composed by two tones, with frequencies $f_{\rm AG} = f_o$ and $f_p = f_o + \Delta f$. However, due to the small amplitude of the current generator, no harmonic components of the tone at frequency f_p have to be considered. Since in this case the frequency basis contains only 9 time varying and one dc components, and the number of considered nodes is smaller, the computational cost is considerably smaller and the method based on the perturbation generator is preferred.

The amplitude of the Nth harmonic component of the self-oscillation signal is easily set by means of the auxiliary generator. In order to be able to evaluate the amplitude of the Mth harmonic component of the reference signal separately from the Nth harmonic component of the autonomous signal, the frequency of the input signal is slightly modified to $f_r = 4.99$ GHz, sufficiently close to 5 GHz to ensure that the impedances seen at the frequencies $M \times f_r = 3 \times f_r = 14.97$ GHz and $N \times f_o = 5 \times f_o = 15$ GHz are nearly the same.

TABLE I
HARMONIC CONTENT OF THE FOUR DIFFERENT RSOS

	C_1	C_2	C_3	C_4
$V_o^N\ (mV)$	60	60	50	40
$V_r^M\ (mV)$	8	11	12	11

III. ANALYSIS OF THE RSO LOCKING RANGE

The parameters of the multiharmonic load have been modified in order to design four different RSO circuits C_1, C_2, C_3, and C_4, with the harmonic content indicated in Table I.

The synchronization bandwidth of the RSO has been analyzed versus the harmonic content of the circuit by tracing the corresponding synchronization loci. The setup of the analysis is based on a single-tone harmonic balance implementation with fundamental frequency $f_b = f_o/M = f_r/N = 1$ GHz, taking into account $M \times N$ harmonics [8]. In this frequency basis,

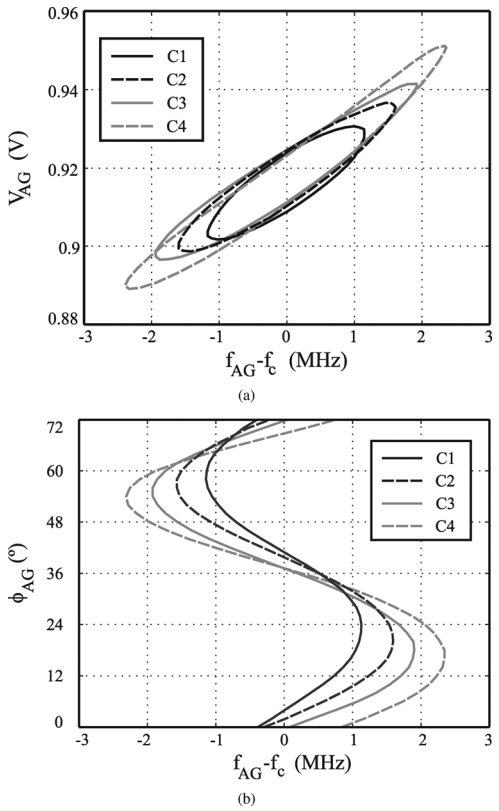

Fig. 4. Synchronized solutions of the four RSOs with different harmonic content in terms of the first harmonic component of the autonomous signal. (a) Amplitude. (b) Phase. Note that the maximum phase variation is $360°/N = 72°$. The power of the reference signal is $P_r = -10$ dBm in all cases.

the frequencies of the autonomous and reference signals are expressed as $f_o = M \times f_b = 3 \times f_b = 3$ GHz and $f_r = N \times f_b = 5 \times f_b = 5$ GHz, respectively, and the synchronizing harmonics are located at $M \times N \times f_b = 15$ GHz.

The synchronization loci represent all of the solutions in which the frequency of the Nth harmonic component of the autonomous signal and the Mth harmonic component of the reference signal are equal and, thus, the phase difference between them $\Delta\phi = \phi_{V_o^N} - \phi_{V_r^M}$ is constant in time. These synchronized solutions can be found by sweeping the value of the variable $\Delta\phi$ between 0° and 360°, calculating for each point of the sweep the values of $f_{\rm AG}$ and $V_{\rm AG}$ for which the non-perturbation condition of the auxiliary generator is satisfied [11]–[13]. Since the value of $\phi_{V_r^M}$ can be assumed constant, the sweep can be realized by varying $\phi_{V_o^N}$ between 0° and 360°, or $\phi_{V_o} = \phi_{AG}$ between 0° and $360°/N = 72°$. The result of this analysis is shown in Fig. 4, in which the amplitude $V_{\rm AG} = V_o$ (a) and the phase $\phi_{AG} = \phi_{V_o}$ (b) have been represented versus the frequency of the output (autonomous) signal. Note that, under rational synchronization, $f_r = N/M \times f_o$. For ease of comparison, the four synchronization loci have been normalized with respect to their center frequency f_c. As can be deduced from the information represented in Fig. 4 and Table I, the locking range increases in the same proportion as the amplitude of the Mth harmonic component of the reference signal, remaining almost constant V_o^N (C_2 with respect to C_1). Otherwise, if V_r^M remains almost constant, the synchronization bandwidth increases in the same proportion as the amplitude of the Nth harmonic component of the autonomous signal decreases (C_3 and C_4 with respect to C_2). The maximun phase change experienced by the fundamental harmonic of the autonomous signal is $360°/N = 72°$, which corresponds to a phase change of 360° in its Nth harmonic component. Note that the tilt angle of all of the synchronization loci is very similar, which means that the quality factor of the four oscillator circuits is nearly the same.

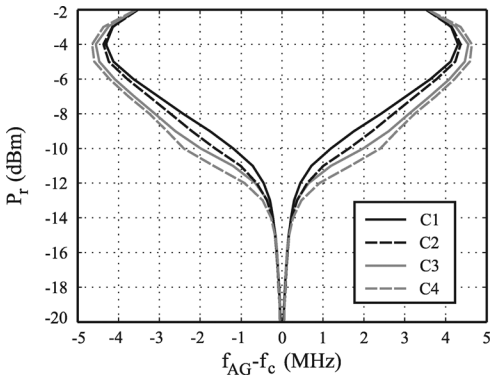

Fig. 5. Arnold tongues of the four RSO circuits with different harmonic content.

The influence of the reference signal power on the synchronization bandwidth is analyzed by tracing the Arnold tongue of the circuits. This representation is achieved by plotting the limits of the locking range versus the power of the reference signal. The Arnold tongues of the four RSO circuits with different harmonic content have been represented in Fig. 5. As can be observed, unlike fundamentally synchronized oscillators, there is a power value for which the locking range of the four RSO circuits presents a maximum, as has been described in the case of harmonically synchronized oscillators ($M = 1$, $N > 1$) [23]. Beyond this point, the locking range of the four RSO circuits tends to be equal. Note that the quality factor and the harmonic content of the RSO circuits have been imposed when the reference signal power is $P_r = -10$ dBm. For other power values, these parameters may suffer slight variations that affect the expected behavior. As a consequence, for input power values greater than -10 dBm, the locking range ratio of the four RSO circuits is not exactly the same as obtained with $P_r = -10$ dBm.

IV. Behavior of the RSO With High Reference Signal Power

When the reference signal power is lower than the value for which the maximum locking range is reached, the synchronization bandwith is delimited by two saddle-node bifurcations. Here, it will be shown that for higher values of the reference signal power, additional saddle-node and inverse Hopf bifurcation points determine the nonlinear dynamics and the behavior of the RSO circuit.

Fig. 6 represents the synchronized solutions of the C_1 circuit in terms of the amplitude $V_{\rm AG}$ and phase $\phi_{\rm AG}$ of the fundamental harmonic component of the autonomous signal. Since the synchronization is realized through the Nth harmonic component of the autonomous signal, the representation of $V_{\rm AG}$ with

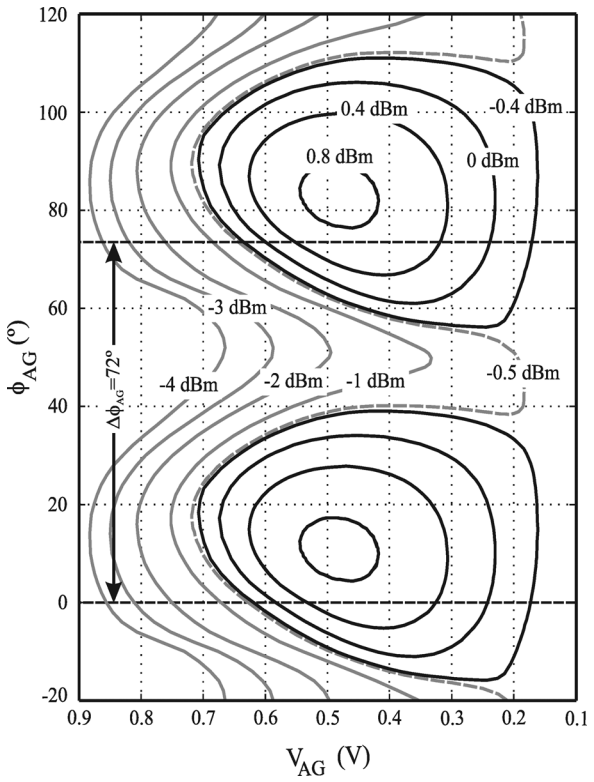

Fig. 6. Synchronized solutions in terms of $V_{\rm AG}$ and $\phi_{\rm AG}$, with high reference signal power. Continuous grey line: Solutions for which all phase values contained within the interval $\phi_{\rm AG} = [0^\circ, 72^\circ]$ are possible. Continuous black line: solutions for which not all the phase values are possible. Dashed gray line: synchronized solutions associated with the boundary reference power $P_r = -0.5$ dBm between the two regions. The period of all of the traces is 72°.

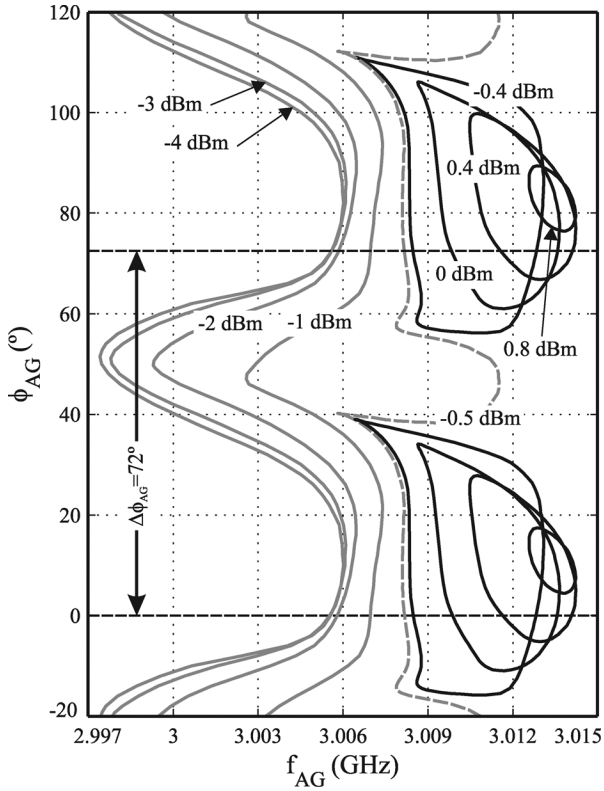

Fig. 7. Synchronized solutions in terms of $f_{\rm AG}$ and $\phi_{\rm AG}$, with high reference signal power. Continuous gray line: solutions for which all phase values contained within the interval $\phi_{\rm AG} = [0^\circ, 72^\circ]$ are possible. Continuous black line: solutions for which not all of the phase values are possible. Dashed gray line: synchronized solutions associated with the boundary reference power $P_r = -0.5$ dBm between the two regions. The period of all of the traces is 72°.

respect to ϕ_{AG} is periodic, with period $360^\circ/N = 72^\circ$. As the reference signal power increases, the mean and the minimum values of $V_{\rm AG}$ decrease. As can be observed, the minimum value of $V_{\rm AG}$ is always reached around the same range of values of $\phi_{\rm AG}$. If the input signal power is greater than -0.5 dBm, a set of values of $\phi_{\rm AG}$ within the range $\phi_{\rm AG} = [0^\circ, 72^\circ]$ for which no synchronized solutions exist. Note that these points are located around the value of ϕ_{AG} for which the minimum of $V_{\rm AG}$ is reached for lower reference signal power. In addition, the width of the subinterval of $\phi_{\rm AG} = [0^\circ, 72^\circ]$ for which no synchronized solutions exist increases with the input signal power. This is due to the fact that the mean value of $V_{\rm AG}$ is reduced when the input power is increased, and there is a minimum value $V_{\rm AG,min}$ below which the existence of synchronized solutions is not possible. As a consequence, the periodic traces of $V_{\rm AG}$ versus ϕ_{AG} are no longer continuous and twist on themselves to form closed loops when the power of the input signal is greater than -0.5 dBm.

From the data displayed in Fig. 6, it is derived that, for high values of P_r, not all the points of the interval $\phi_{\rm AG} = [0^\circ, 72^\circ]$ are associated with synchronized solutions. Therefore, the phase difference between the RSO autonomous signal and the reference signal cannot take all of the theoretical values. Fig. 7 shows the phase of the RSO autonomous signal, referred to the reference signal. For $P_r \leq -0.5$ dBm the traces are continuous and all of the values of phase are possible. Otherwise, if $P_r > -0.5$ dBm, the curves form closed loops, since it is not possible to reach synchronized solutions for all of the phase values. Notice that, as the reference signal power increases, the center frequency of the synchronization loci is considerably modified. This is due to the fact that the power of the reference signal takes values sufficiently high to affect the frequency $f_o = f_{\rm AG}$ (and the amplitude $V_o = V_{\rm AG}$) of the autonomous signal. However, unlike the case of fundamentally synchronized oscillators, the autonomous signal is not extinguished through an inverse Hopf bifurcation because its frequency is not close to that of the reference signal.

The synchronized solutions associated with the continuous traces represented in Figs. 6 and 7, with $P_r \leq -0.5$ dBm, are found by sweeping the phase of the auxiliary generator and calculating the values of $f_{\rm AG}$ and $V_{\rm AG}$ for which the nonperturbation condition is fulfilled. However, this method is not suitable to calculate the synchronized solutions with $P_r > -0.5$ dBm. On the one hand, since the traces of $\phi_{\rm AG}$ versus $f_{\rm AG}$ form closed loops, there are two possible values of $V_{\rm AG}$ and $f_{\rm AG}$ for which the nonperturbation condition of the auxiliary generator is satisfied, and the optimization methods provided by the used commercial sofware package are unable to simultaneously find them. On the other hand, the range of the inverval $\phi_{\rm AG} = [0^\circ, 72^\circ]$ which is not associated to synchronized solutions is unknown *a priori*. Thus, when trying to perform the sweep between 0° and $360^\circ/N = 72^\circ$, the optimization method

fails to converge at the points in which no synchronized solution exists. In order to obtain these particular synchronized solutions, a triple sweep is performed over the phase $\phi_{\rm AG}$, the amplitude $V_{\rm AG}$ and the frequency $f_{\rm AG}$ of the auxiliary generator. Since a synchronized operation regime is assumed, the frequency of the reference signal is expressed as $1/r \times f_o$. For each point of the sweep, the admittance seen by the auxiliary generator $Y_{\rm AG}(\phi_{\rm AG},\, V_{\rm AG},\, f_{\rm AG}) = I_{\rm AG}/V_{\rm AG}$ is calculated, and then, the sets $(\phi_{{\rm AG},k},\, V_{{\rm AG},k},\, f_{{\rm AG},k})$ for which zero admittance is obtained are found. Since the admittance seen by the auxiliary generator at these points is zero $Y_{\rm AG}(\phi_{{\rm AG},k},\, V_{{\rm AG},k},\, f_{{\rm AG},k}) = 0$, the nonperturbation condition of the auxiliary generator is fulfilled, and the set $(\phi_{{\rm AG},k},\, V_{{\rm AG},k},\, f_{{\rm AG},k})$ represents a synchronized solution.

A. *Stability of the Synchronized Solutions*

The stability of the synchronized solutions represented in Figs. 6 and 7 has been determined through the envelope transient technique. With the data provided by this analysis, the Poincare maps of the amplitude $V_{\rm AG}$ and phase $\phi_{\rm AG}$ of the autonomous signal have been depicted [13].

To determine the stability of the synchronized solutions, a previous step is performed to ensure the existence and the stability of the autonomous signal. Without connecting the auxiliary generator to the circuit, the trivial dc solution is perturbed with a time domain defined low amplitude current pulse. After switching off the perturbation, the time evolution of the system state variables is determined through the Envelope Transient technique. As long as the system evolves towards the desired autonomous solution and the simulation parameters have been conveniently chosen, the stability of the harmonic balance predicted autonomous solution can be ensured [14]. After that, a sweep is performed on the frequency of the reference signal f_r. At each point of the sweep, the auxiliary generator, with frequency $f_{\rm AG} = f_o$ and amplitude $V_{\rm AG} = V_o$, is connected to the circuit during a short time to initialize the state variables of the oscillator [15], [18]. After disconnecting the auxiliary generator, the state variables of the system evolve in time towards a stable steady state solution. Note that the envelope transient technique is suitable to efficiently obtain unsynchronized quasi-periodic solutions. In addition, inverse Hopf bifurcation points can be identified, since the envelope transient technique is also able to detect the evolution of the autonomous signal to zero amplitude [13], [17].

When the RSO works under a rational synchronization regime, the relation $r = M/N = f_o/f_r$, with $M,\, N \in \mathbb{N}$, is satisficed. Therefore, the frequency of the synchronizing harmonics is identical $N \times f_o = M \times f_r$ and no low-frequency mixing signal between them is generated. Thus, the amplitude of all of the harmonic components of the autonomous signal is constant in time. In addition, since the phase difference between the synchronizing harmonics is fixed, the phase difference between the circuit output signal and the reference signal is also constant and known. Because the amplitude and phase of a synchronized solution are constant in time, they appear as a point in the Poincare map. Otherwise, if the values of P_r and f_r do not ensure the fulfillment of $r = M/N = f_o/f_r$, the circuit shows a quasiperiodic steady-state solution. Since the relation

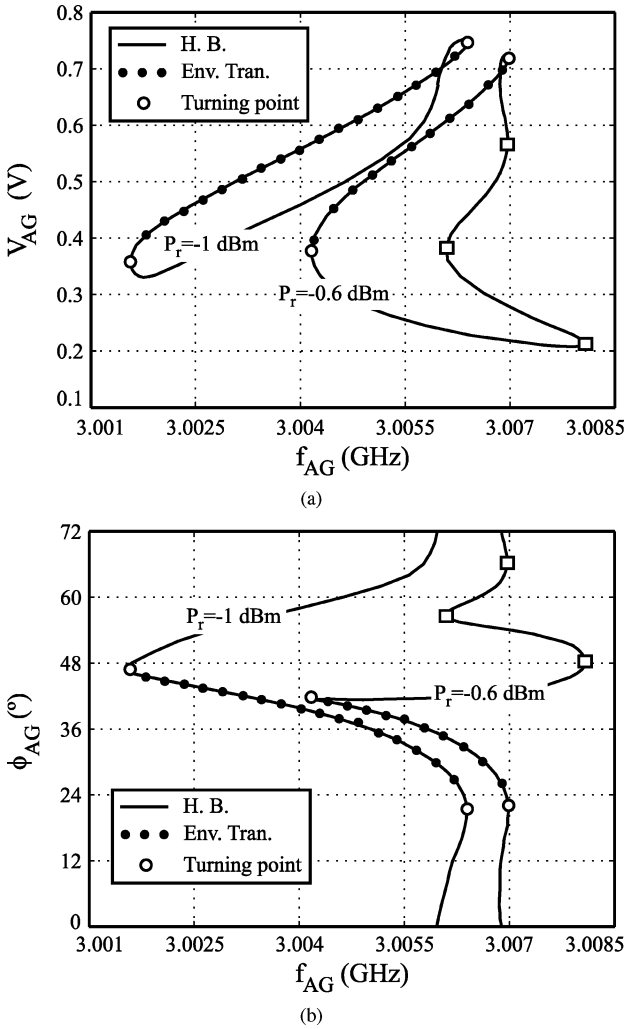

Fig. 8. Synchronized solutions with $P_r = -1$ dBm and $P_r = -0.6$ dBm, in terms of (a) $V_{\rm AG}$ and (b) $\phi_{\rm AG}$. Gray line: harmonic balance data. Black points: envelope transient data. White circles: turning points which delimit the stable locking range. Square markers: other turning points. The envelope transient data corresponding to unsynchronized solutions are not represented.

$N \times f_o = M \times f_r$ is not satisfied, a low-frequency mixing signal that modulates the amplitude of all of the harmonic components of the autonomous signal is generated. In this way, an unsynchronized solution is represented in the Poincare map as a vertical line, because of the time variation of the state variables.

The power of the reference signal has been divided in two regions around the limit value $P_r = -0.5$ dBm associated with the change from continuous traces to closed loops. Fig. 8 shows the synchronization loci obtained for $P_r = -1$ dBm and $P_r = -0.6$ dBm in terms of (a) $V_{\rm AG}$ and (b) $\phi_{\rm AG}$. The represented data has been calculated with the harmonic balance and envelope transient techniques. In the case of $P_r = -1$ dBm, which can be considered far enough from the limit value $P_r = -0.5$ dBm, the locking range is delimited by two saddle-node bifurcations, since the Jacobian matrix associated with the system becomes singular at those points. However, when the reference signal power is $P_r = -0.6$ dBm, the synchronization locus presents some additional turning points, and, thus, its shape is not elliptical. Although all of the

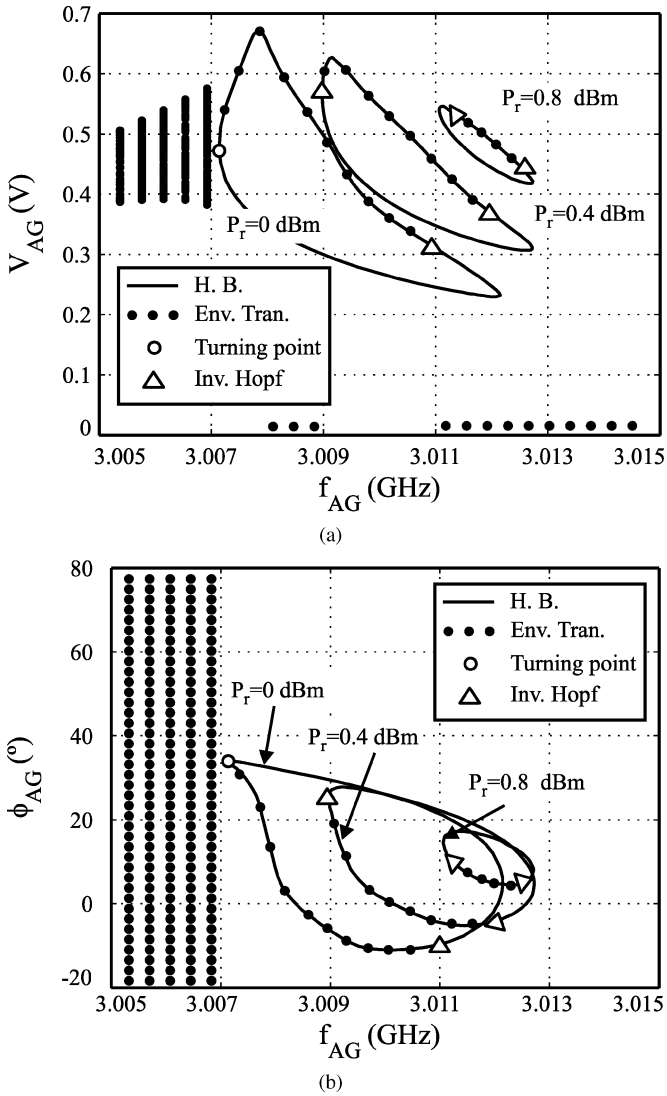

Fig. 9. Synchronized solutions with $P_r = 0$ dBm, $P_r = 0.4$ dBm and $P_r = 0.8$ dBm, in terms of (a) $V_{\rm AG}$ and (b) $\phi_{\rm AG}$. Gray line: harmonic balance data. Black points: envelope transient data. White circle: turning point which delimits the stable locking range. Triangle markers: inverse Hopf bifurcation points.

points within the interval $\phi_{AG} = [0°, 72°]$ are associated with both stable and unstable synchronized solutions, the shape of the representation of $\phi_{\rm AG}$ versus $f_{\rm AG}$ is also conditioned by the presence of more than two turning points. The associated Poincare map has been superimposed on the data provided by the harmonic balance simulations. As can be observed, despite the shape of the synchronization locus, the stable locking range is delimited by two saddle-node bifurcations, as is usual in synchronized oscillators. Note that the stable part of the locking range decreases as the reference signal power increases, which agrees with the harmonic synchronization theory [23]. For the sake of clarity, the Poincare maps of the unsynchronized solutions have not been depicted in the figure.

On the other hand, the synchronization loci obtained with input power values $P_r = 0, 0.4$, and 0.8 dBm are represented in Fig. 9. In this case, the power of the reference signal is greater than $P_r = -0.5$ dBm and the common feature of all synchronized solutions is the fact that not all of the points contained on the interval $\phi_{\rm AG} = [0°, 72°]$ are associated with synchronized solutions. When the reference signal power is $P_r = 0$ dBm, the stable locking range is delimited by two different bifurcations. If the frequency of the reference signal is on the left side of the synchronization locus, the Poincare map shows a typical quasiperiodic regime in which the condition of rational synchronization $r = f_o/f_r = M/N$ is not fulfilled. Therefore, $V_{\rm AG}$ is not constant in time and $\phi_{\rm AG}$ is continuously increasing (or decreasing), meaning that the locking range is delimited by a saddle-node bifurcation on its left side. However, if the frequency of the reference signal moves on the right side of the synchronization locus, the Poincare map shows a solution in which the autonomous signal has zero amplitude $V_{\rm AG} = 0$, which means that this signal has been extinguished via an inverse Hopf bifurcation. Note that the inverse Hopf bifurcation is reached before the locking range corner predicted by the harmonic balance technique. For higher values of P_r, the stable locking range is delimited by two inverse Hopf bifurcations. From this analysis, it follows that, in an RSO circuit with high input power, the extinction of the autonomous signal through an inverse Hopf bifurcation is conditioned by the power and the frequency of the reference signal, and by the phase difference between the reference and the autonomous signal. Beyond this point, since the only signal present in the circuit is the reference, the steady-state solution becomes nonautonomous and periodic.

Note that the center frequency of the synchronization loci represented in Figs. 8 and 9 depends on the reference signal power. Although the frequency $f_r \approx 5$ GHz of the reference signal is not close to the autonomous signal $f_0 \approx 3$ GHz, its power P_r is high enough in order to have a great influence on the parameters of the autonomous signal.

B. Global Behavior of the RSO

Fig. 10 combines the data represented in Figs. 6–9 and shows the evolution of the synchronized solutions of the RSO circuit in terms of the three involved variables, $f_o = f_{\rm AG}$, $\phi_o = \phi_{\rm AG}$, and $V_o = V_{\rm AG}$. The stable part of the synchronization loci is indicated, together with the different bifurcation points which determine the nonlinear dynamics of the circuit when high values of reference signal are considered. The stable part of the synchronization loci corresponding with $P_r = -2$ dBm and $P_r = -1$ dBm is delimited by two saddle-node bifurcations (turning points). As was represented in Fig. 8, all the theoretical phase change values are possible and the synchronization loci are elliptically shaped. In the case of $P_r = -0.6$ dBm, all phase change values are still possible, but the synchronization locus presents more than two turning points, which determine its particular profile. Note that the stable part of the synchronization locus is enclosed by only two turning points. For higher values of the reference signal power, $P_r > -0.5$ dBm, not all of the points contained in the range $\phi_{\rm AG} = [0°, 72°]$ are associated with synchronized solutions. The stable part of the solution corresponding to $P_r = 0$ dBm is bounded on its right hand side by a turning point and by an inverse Hopf bifurcation on its left hand side. When $P_r > 0$ dBm, only inverse Hopf bifurcation points are present. Due to the fact that the synchronized solutions are represented in terms of the fundamental harmonic component

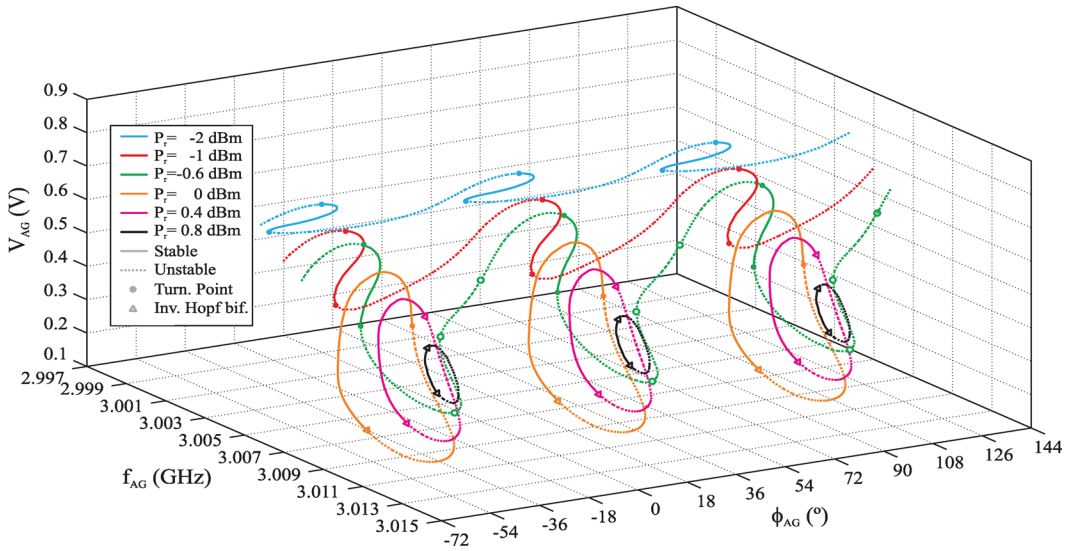

Fig. 10. Evolution of the synchronized solutions of the RSO versus the reference signal power P_r. The solutions are represented in terms of the three involved state variables $f_o = f_{\rm AG}$, $V_o = V_{\rm AG}$ and $\phi_o = \phi_{\rm AG}$. Continuous line: stable solutions. Dashed line: unstable solutions. Filled circle marker: turning points which delimit the stable region. Unfilled circle marker: other turning points. Triangle marker: inverse Hopf Bifurcation points.

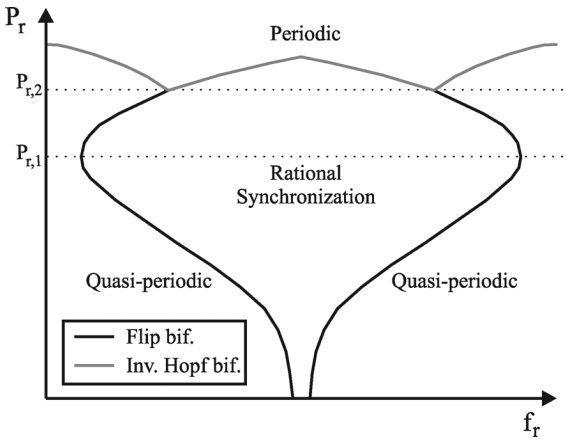

Fig. 11. Scheme of the whole behavior of the RSO, as a function of the frequency f_r and the power P_r of the reference signal. Note that the frequency of the autonomous signal is expressed as $f_o = f_{\rm AG} = r \times f_r$.

of the autonomous signal, all the curves exhibit a periodicity of $360°/N = 72°$.

The whole behavior of the RSO locking range, as a function of the frequency f_r and the power P_r of the reference signal, is schematized in Fig. 11. $P_{r,1} \approx -4$ dBm is the power value for which the maximum synchronization bandwidth is reached. If the power of the reference signal is less than this value, the operation regime is similar to the fundamental synchronization, in which the stable locking range is delimited by two saddle-node bifurcation points. When the power of the reference signal is between $P_{r,1}$ and $P_{r,2} \approx 0$ dBm, the stable synchronization bandwidth reduces as the reference power increases. In this region, the stable locking range is still delimited by two saddle-node bifurcations, but the synchronization loci present some additional turning points which determine their shape, as was represented in Fig. 8. For input power values greater than $P_{r,2}$, the locking range is delimited by two inverse Hopf bifurcations and the points contained in an subinterval of the range $\phi_{\rm AG} = [0°,\ 72°]$, which increases with the reference signal power, are not associated with synchronized solutions.

V. Experimental Results

A. Implementation

The RSO circuit corresponding to C_4 trace in Fig. 4 has been manufactured in microstrip technology. The selected substrate is ARLON 25N, with relative dielectric constant $\epsilon_r = 3.38$- and 0.75-mm thickness. This commercially available substate is well modeled at the frequencies of interest, from 3 to 15 GHz. However, the values of its dielectric permittivity and conductivity at the desired frequencies have been verified in the facilities of TSC-UNIOVI Laboratory, through a 85072A series Agilent Split Cylinder Resonator and a 85070E series Agilent Dielectric Probe Kit. The circuit has been manufactured by using a high precision Protolaser S series LPKF structuring machine. Therefore, the errors in the microstrip lines dimensions are minimized.

Since all of the passive subnetworks, i.e., filters, multiharmonic load, dc-bias, and feedback networks, are implemented using distributed elements, the required number of components is very reduced.

Multiharmonic load parameters are used as optimization variables along the entire design process. Its input impedance $Z_L(f)$ determines the amplitude V_o and the frequency f_o of the autonomous signal, as well as the quality factor Q_L and the harmonic content of the circuit. In order to be able to accurately control the input impedance $Z_L(f)$ at frequencies f_o and f_r, and their harmonic components, a structure based on an arbitrarily width modulated microstrip line is used [20]. The proposed structure allows the control of its impedance around different non harmonically related frequencies. In addition, this control can be applied over a fairly large bandwidth around each considered frequency point. These particular features make the structure also suitable for the implementation of the DC-bias

networks, with high input impedance at $k \times f_o$ and $j \times f_r$ GHz, with $k = \{1, \ldots, N\}$ and $j = \{1, \ldots M\}$.

At the end of the design process, the frequency response of all of the passive networks has been calculated in an electromagnetic simulation based on the Method of Moments (MoM). The information provided by this analysis has been used to slightly correct such networks, in order to avoid undesired deviations which could affect the performance of the circuit. Moreover, the inclusion of a varactor diode as a part of the feedback network allows the correction of small deviations on the performance of the manufactured circuit which could be still observed at the experimental stage due to a great variety of effects that cannot been taken into account along the design process [10].

B. Measurements

The RSO has been characterized by means of an Agilent PNA-X series vector network analyzer. For a configurable power value P_r of the reference signal, which is generated by the PNA-X, the frequency f_r can be automatically swept between the desired limits. At each point of the sweep, the power and the phase of the output signal, with frequency $f_o = M/N \times f_r$ (under rational synchronization operation regime), are measured and related to the corresponding parameters of the reference signal. In this way, the synchronization loci, measured at the RSO output port, are automatically traced.

The measured synchronized solutions, in terms of the output signal, are represented in Fig. 12, together with the data provided by harmonic balance-based simulations. Fig. 12(a) shows the variation of the output signal power versus the autonomous signal frequency. The measured phase change between the output and input signals is depicted in Fig. 12(b). For ease of comparison, the synchronization loci have been normalized with respect to their center frequency f_c and the phase change traces have been modified to achieve zero variation at the center frequency of each locus. The maximun measured phase change is about 30°, which is near to the theoretical limit value $72/2 = 36°$. This maximum value cannot be reached because of nonlinear effects associated with noise amplification that are observed in synchronized oscillators working near the locking range corners [7]. The measured behavior of the RSO locking range versus the reference signal power is depicted in Fig. 13. The good agreement between the simulation provided data and measurements validates the synchronization bandwidth optimization technique and the existence of a maximum stable locking range value versus the reference signal power.

Since one goal of the rational synchronization process is the low cost generation of carriers with good phase noise properties, this feature has also been measured. The PNA-X has been configured to generate a reference signal with power $P_r = -10$ dBm. The frequency of this signal is selected in order to ensure that the working point of the RSO is about the center of the corresponding synchronization locus $f_r = f_c$. The phase of the RSO output signal $\phi_{out}(f_r = f_c,\, t)$ is measured and stored during a long time interval. The phase noise is then directly calculated as the power spectral density of the time dependent RSO output signal phase. The same procedure has been applied to characterize the phase noise of the reference signal. In the case of the free running oscillator, the main contribution to the phase

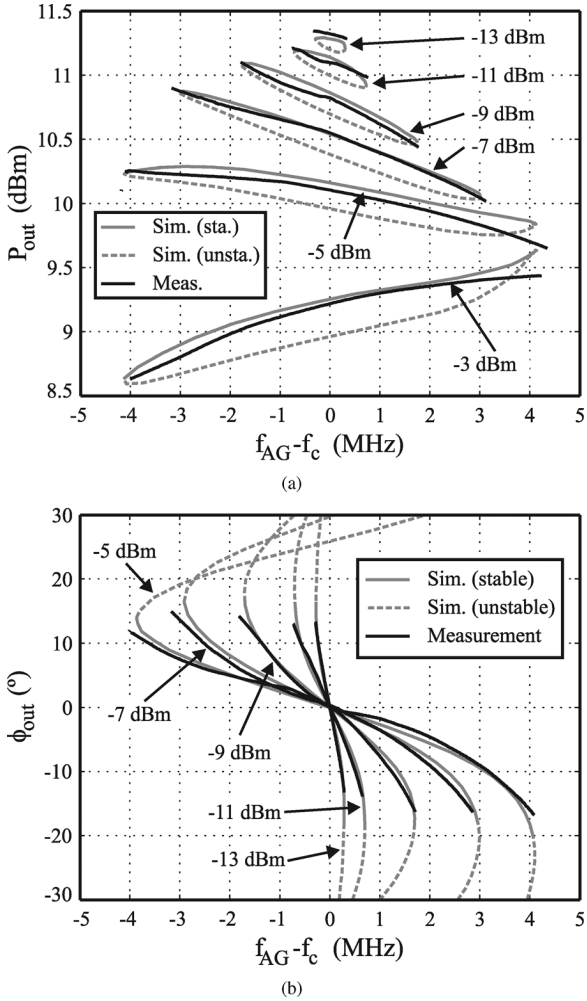

Fig. 12. Measured synchronized solutions in terms of the output signal. (a) Power. (b) Phase change. Continuous gray line: stable simulated solutions. Dashed gray line: unstable simulated solutions. Black line: measurements. The phase change trace corresponding to $P_r = -3$ dBm has not been represented because it is very similar to that obtained with $P_r = -5$ dBm. Note that the frequency of the reference signal is given by $f_r = M/N \times f_o$.

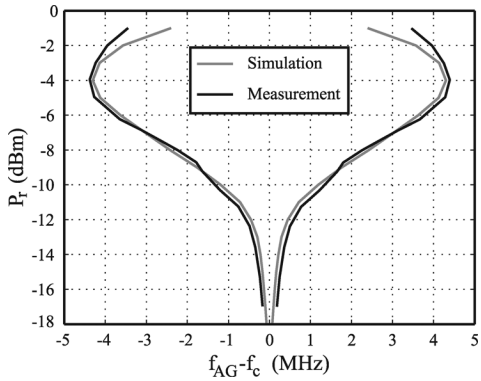

Fig. 13. Experimental Arnold tongue of the implemented circuit. Gray line: simulation data. Black line: measurements.

noise near to the carrier is the frequency variation of the autonomous signal [27]. Therefore, the described method does not provide accurate results because constant frequency operation cannot be assumed. To overcome that problem, the phase noise of the free running oscillator has been characterized through

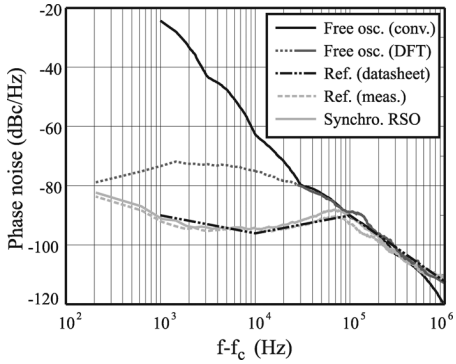

Fig. 14. Measured phase noise. Continuous black line: free-running oscillator. Dashed black line: Reference signal source (datasheet). Dashed gray line: reference signal power (measured), with $P_r = -10$ dBm. Continuous gray line: synchronized RSO, with $P_r = -10$ dBm. The dotted line corresponding to the free running oscillator represents the wrong data provided by the discrete Fourier transform (DFT) method.

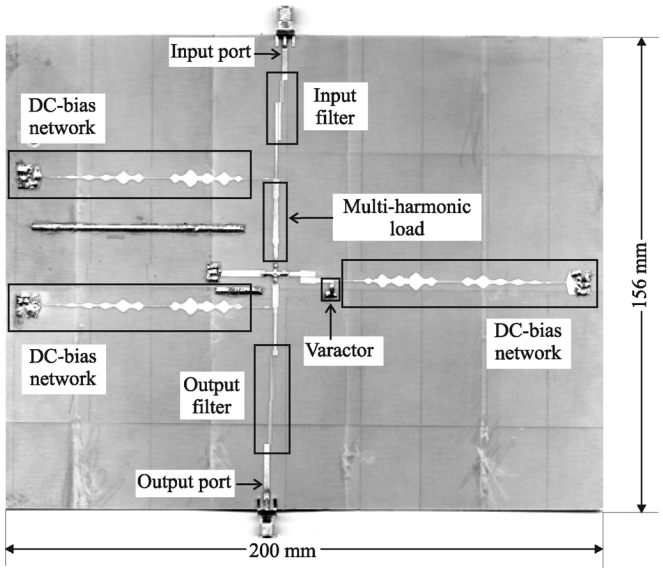

Fig. 15. Picture of the manufactured prototype. All of the basic subnetworks are indicated, including the multiharmonic load and dc-bias networks, based on arbitrarily width modulated microstrip lines.

the estimation of the amplitude noise to phase noise conversion, which is performed through the FS-K4 commercial software, implemented over an FSP-series Rhode-Schwarz spectrum analyzer. The obtained results are represented in Fig. 14, together with the typical phase noise behavior of the synchronization source, provided by the manufacturer. As can be observed, under rational synchronization regime, the phase noise of the oscillator is considerably improved, since it is similar to that of the reference source. Note that, when measuring the free-running oscillator phase noise, the two proposed methods provide similar results when the measuring frequency point is far away from the carrier, approximately $f - f_c > 2 \times 10^4$ Hz. In addition, since the phase noise measurement of the reference signal source agrees with the data provided by the manufacturer, the proposed method is validated.

Finally, Fig. 15 shows a picture of the manufactured prototype, in which the layout of the multiharmonic load and dc-bias networks can be observed.

VI. Conclusion

An in-depth analysis of the behavior of a rationally synchronized oscillator with $r = M/N = 3/5$ has been presented. The synchronization bandwidth of the circuit has been optimized through a technique based on the control of its harmonic content. The obtained data show that the locking range is proportional to the amplitude of the Mth harmonic component of the reference signal, and inversely proportional to the Nth harmonic component of the autonomous signal. In addition, it exhibits a maximum versus the reference signal power. The locking range of the RSO has been analyzed in detail, versus the reference signal power, through harmonic balance and envelope transient techniques. For high reference signal power values, the stable locking range reduces as the input power increases and the circuit dynamics is conditioned by the presence of several saddle-node bifurcation points. If the input power continues to increase, the stable locking range is delimited by inverse Hopf bifurcation points and not all the phase change values are possible. A prototype has been implemented and characterized, demonstrating a good agreement with simulation data.

References

[1] S. Ver Hoeye, M. Gonzalez, M. Fernandez, C. Vazquez, L. F. Herran, and F. Las Heras, "Harmonic optimization of rationally synchronized oscillators," *IEEE Microw. Wireless Compon. Lett.*, vol. 19, no. 5, pp. 317–319, May 2009.

[2] H. C. Chang, A. Borgioli, A. P. Yeh, and R. A. York, "Analysis of oscillators with external feedback loop for improved locking range and noise reduction," *IEEE Trans. Microw. Theory Tech.*, vol. 47, no. 8, pp. 1535–1543, Aug. 1999.

[3] S. Ver Hoeye, L. Gutierrez, S. Sancho, A. Suarez, and P. Gonzalez, "Sub-harmonic and rational synchronization for phase-noise improvement," in *Proc. 31st Eur. Microw. Conf.*, London, U.K, Sep. 2001, vol. 1, pp. 237–240.

[4] F. Ramirez, M. E. de Cos, and A. Suarez, "Nonlinear analysis tools for the optimized design of harmonic-injection dividers," *IEEE Trans. Microw. Theory Tech.*, vol. 51, no. 6, pp. 1752–1762, Jun. 2003.

[5] M. E. de Cos, F. Ramirez, and A. Suarez, "Multi-harmonic generator based on the synchronization of a nonlinear bipolar transistor," in *IEEE MTT-S Int. Microw. Symp. Dig.*, Philadelphia, PA, Jun. 2003, vol. 1, pp. 2177–2180.

[6] M. Fernandez, S. Ver Hoeye, C. Vazquez, G. R. Hotopan, R. Camblor, and F. Las Heras, "Design and analysis of a multi-carrier Tx-Rx system based on rationally synchronized oscillators for localization applications," *Progr. Electromagn. Res.*, vol. 120, pp. 1–16, 2011.

[7] S. Ver Hoeye, A. Suarez, and S. Sancho, "Analysis of noise effects on the nonlinear dynamics of synchronized oscillators," *IEEE Microw. Wireless Compon. Lett.*, vol. 11, no. 9, pp. 376–378, Sep. 2001.

[8] M. Fernandez, S. Ver Hoeye, C. Vazquez, G. R. Hotopan, R. Camblor, and F. Las Heras, "Optimization of the synchronization bandwidth of rationally synchronized oscillators based on bifurcation control," *Progr. Electromagn. Res.*, vol. 119, pp. 299–313, 2011.

[9] H. Jiang and R. Penno, "Effects of amplitude dynamics on beam steering and shaping in coupled oscillator array," *IEEE Antennas Wireless Propag. Lett.*, vol. 9, no. 5, pp. 474–477, May 2010.

[10] H. Jiang, R. Ordonez, and R. Penno, "Analysis of synchronized coupled oscillators with application to radar beam scanning," *Control Eng. Practice*, vol. 18, pp. 1379–1385, Aug. 2010.

[11] S. Ver Hoeye, L. Zurdo, and A. Suarez, "New nonlinear design tools for self-oscillating mixers," *IEEE Microw. Wireless Compon. Lett.*, vol. 11, no. 8, pp. 337–339, Aug. 2001.

[12] S. Ver Hoeye, F. Ramirez, and A. Suarez, "Nonlinear optimization tools for the design of high-efficiency microwave oscillators," *IEEE Microw. Wireless Compon. Lett.*, vol. 14, no. 5, pp. 189–191, May 2004.

[13] S. Ver Hoeye, L. F. Herran, M. Fernandez, and F. Las Heras, "Design and analysis of a microwave large-range variable phase-shifter based on an injection-locked harmonic self-oscillating mixer," *IEEE Microw. Wireless Compon. Lett.*, vol. 16, no. 6, pp. 342–344, Jun. 2006.

[14] E. Ngoya and R. Larcheveque, "Envelop transient analysis: A new method for the transient and steady-state analysis of microwave communication circuits and systems," in *IEEE MTT-S Int. Microw. Symp. Dig.*, Jun. 1996, vol. 3, pp. 1365–1368.
[15] E. de Cos, A. Suarez, and S. Sancho, "Envelope transient analysis of self-oscillating mixers," *IEEE Trans. Microw. Theory Tech.*, vol. 52, no. 4, pp. 1090–1100, Apr. 2004.
[16] A. Collado, F. Ramirez, A. Suarez, and J. P. Pascual, "Harmonic-Balance analysis and synthesis of coupled-oscillator arrays," *IEEE Microw. Wireless Compon. Lett.*, vol. 14, no. 5, pp. 192–194, May 2004.
[17] A. Collado and A. Suarez, "Application of bifurcation control to practical circuit design," *IEEE Trans. Microw. Theory Tech.*, vol. 53, no. 9, pp. 2777–2788, Sep. 2005.
[18] A. Georgiadis, A. Collado, and A. Suarez, "New techniques for the analysis and design of coupled-oscillator systems," *IEEE Trans. Microw. Theory Tech.*, vol. 54, no. 11, pp. 3864–3877, Nov. 2006.
[19] L. F. Herran, S. Ver Hoeye, and F. Las Heras, "Nonlinear optimization tools for the design of microwave high-conversion gain harmonic self-oscillating mixers," *IEEE Microw. Wireless Compon. Lett.*, vol. 16, no. 1, pp. 16–18, Jan. 2006.
[20] S. Ver Hoeye, C. Vazquez, M. Gonzalez, M. Fernandez, L. F. Herran, and F. Las Heras, "Multi-harmonic DC-bias network based on arbitrarily width modulated microstrip line," *PIER Lett.*, vol. 11, pp. 119–128, 2009.
[21] F. Ramirez, M. Ponton, S. Sancho, and A. Suarez, "Phase-noise analysis of injection-locked oscillators and analog frequency dividers," *IEEE Trans. Microw. Theory Tech.*, vol. 56, no. 2, pp. 393–407, Feb. 2008.
[22] I. Schmideg, "Harmonic synchronization of nonlinear oscillators," *Proc. IEEE*, vol. 59, no. 8, pp. 1250–1251, Aug. 1971.
[23] R. Knoechel and K. Schuenemann, "Noise and transfer properties of harmonically synchronized oscillators," in *IEEE MTT-S Int. Microw. Symp. Dig.*, Jun. 1978, vol. 78, pp. 390–392.
[24] X. Zhang, X. Zhou, and A. S. Daryoush, "A theoretical and experimental study of the noise behavior of subharmonically injection locked local oscillator," *IEEE Trans. Microw. Theory Tech.*, vol. 40, no. 5, pp. 895–902, May 1992.
[25] S. Kudszus, T. Berceli, A. Tessmann, M. Neumann, and W. H. Haydl, "W-band HEMT-oscillator MMICs using subharmonic injection locking," *IEEE Trans. Microw. Theory Tech.*, vol. 48, no. 12, pp. 2526–2532, Dec. 2000.
[26] P. F. Combes, J. Graffeuil, and J. F. Sautereau*, Microwave Components, Devices and Active Circuits*. New York: Wiley, 1987.
[27] A. Suarez, S. Sancho, S. Ver Hoeye, and J. Portilla, "Analytical comparison between time- and frequency-domain techniques for phase-noise analysis," *IEEE Trans. Microw. Theory Tech.*, vol. 50, no. 10, pp. 2353–2361, Oct. 2002.

Miguel Fernández García (M'XX) received the M.Sc. degree in telecommunication engineering and Ph.D. degree from the University of Oviedo, Gijon, Spain, in 2006 and 2010, respectively.

From 2005 to 2008, he was a Research Assistant with the Signal Theory and Communications Area, University of Oviedo, Gijon, Spain, where he is currently an Assistant Professor. His main research effort is focused on nonlinear analysis and optimization of microwave oscillator-based circuits and active and phased antenna arrays.

Samuel Ver Hoeye (M'05) received the M.Sc. degree in electronics engineering from the University of Gent, Gent, Belgium, in 1999, and the Ph.D. degree from the University of Cantabria, Santander, Spain, in 2002.

He is currently an Associate Professor with the Department of Electrical and Electronic Engineering, University of Oviedo, Gijon, Spain. His main research is focused on nonlinear analysis and optimization of microwave circuits and their application to active antennas.

Carlos Vázquez received the M.Sc. degree in telecommunication engineering from the University of Oviedo, Gijon, Spain, in 2007, where he is currently working toward the Ph.D. degree.

Since 2007, he has been a Research Assistant with the Signal Theory and Communications Area, University of Oviedo, Gijon, Spain. His research effort mainly focus on nonlinear analysis and the optimization of microwave circuits to be used in active antennas.

George Roberto Hotopan received the M.Sc. degree in telecommunication engineering from University of Oviedo, Gijon, Spain, in 2010, where he is currently working toward the Ph.D. degree.

Since 2010, he has been a Research Assistant with the Signal Theory and Communications Area, University of Oviedo, Gijon, Spain. His research effort mainly focuses on the design, optimization, and analysis of multifunctional circuits based on oscillators, operating in the millimeter- and submillimeter-wave bands.

René Camblor received the M.Sc. degree in telecommunications engineering from the University of Oviedo, Gijon, Spain, in 2006, where he is currently working toward the Ph.D. degree.

Since 2009, he has been a Research Engineer with the Signal Theory and Communications Area, University of Oviedo, Gijon, Spain. His current research interests are submillimeter-wave antennas and terahertz systems.

Fernando Las Heras (M'86–SM'08) received the M.S. and Ph.D. degrees from the Universidad Politecnica de Madrid, Madrid, Spain, in 1987 and 1990, respectively, both in telecommunication engineering.

From 1988 to 1990, he was a National Graduate Research Fellow. From 1991 to 2000, he was an Associate Professor with the Department of Signals, Systems and Radiocommunications, Universidad Politecnica de Madrid, Madrid, Spain. From 2001 to 2003, he was an Associate Professor with the Department of Electrical Engineering, Unversity of Oviedo, Gijon, Spain, pioneering the Signal Theory and Communications Area. Since December 2003, he has been a Full Professor with the University of Oviedo. His main research interests include the analysis and design of antennas, electromagnetic interference, and the inverse electromagnetics problem with application to diagnostic, measurement, and synthesis of antennas.